The Raman Spectrum and High Lattice Thermal Conductivity of Ternary Layered Boride Cr_3AlB_4

S. Wang[a,b,*], B. Liu[a] and J. Song[a,b]

[a] *School of Mathematics and Physics, Nanyang Institute of Technology, Changjiang Road, No. 80, 473004 Nanyang City, Henan, China*
[b] *Henan Province Engineering Technology Research Center of New Optoelectronic and Storage Materials, Changjiang Road, No. 80, 473004 Nanyang City, Henan, China*

Received: 18.07.2025 & Accepted: 05.11.2025

Doi: 10.12693/APhysPolA.148.228 *e-mail: shengzw@nyist.edu.cn

The Raman spectrum and lattice thermal conductivity of the ternary layered boride Cr_3AlB_4 were investigated using first-principles methods in this study. The results of the electronic band structure indicate that Cr_3AlB_4 exhibits metallic properties. Cr_3AlB_4 also exhibits 9 Raman-active and 12 infrared-active modes. Low- and mid-frequency motions are dominated by Cr and Al displacements, whereas high-frequency modes arise chiefly from B-atom vibrations. The computed lattice thermal conductivity of Cr_3AlB_4 is 87.9 W/(m K); the phonon lifetime is long at low frequencies, while the overall group velocity remains modest. However, the effects of anharmonic vibrations are minimal, as indicated by a small Grüneisen parameter, and the anharmonic scattering rate is also low due to a limited weighted phase space. The elevated thermal conductivity of Cr_3AlB_4 arises from its compact crystal structure, strong covalent bonds, minimal anharmonic vibration effects, and fewer phonon scattering channels.

topics: Cr_3AlB_4, Raman spectrum, lattice thermal conductivity

1. Introduction

In recent years, MAB phase materials have emerged as novel, atomic-layered ternary transition-metal borides. Thanks to the distinctive M–A–B layered architecture, these materials combine metallic and ceramic properties in a single compound. Such a unique structure has attracted widespread attention for mechanical, thermal and high-temperature applications [1–4]. Like MAX phases (where M denotes a transition metal, A is a main-group element, and X is carbon or nitrogen), MAB phases also adopt a layered architecture, conferring a hybrid property set that neither traditional metals nor ceramics can match. Owing to exceptional hardness, fracture toughness, electrical conductivity, and oxidation resistance at elevated temperatures, MAB phases are now contenders for structural parts in harsh environments, high-temperature coatings, and thermal-management devices. Unraveling the link between microstructural architecture and bulk behavior is essential to moving these materials from the promise stage to practice [5, 6].

Lattice thermal conductivity (κ_l) is one of the important physical properties of materials. It determines the efficiency of materials in the heat conduction process and is crucial for understanding the thermal transport mechanism in materials and evaluating their application performance in thermal management, thermoelectric, and other fields [7]. In practical applications, such as heat dissipation of electronic devices and performance optimization of thermoelectric materials, an in-depth understanding and precise regulation of the lattice thermal conductivity of materials are required [8–13]. For MAB materials with potential application value, studying their κ_l helps reveal their thermal transport characteristics and provides theoretical support for their applications in related fields.

Contemporary Raman spectroscopy studies increasingly rely on cutting-edge computational tools, in particular DFT- (density functional theory)-based first-principles modelling. These calculations allow accurate prediction of the phonon spectrum, vibration modes of materials, as well as their corresponding Raman-active peak positions and intensities, thereby providing a solid theoretical basis for the analysis of experimental data [14–18]. First-principles calculations provide an accurate description of the structure and properties of materials at the atomic and electronic levels without relying on experimental data or empirical parameters [19–23]. In the study of κ_l, first-principles calculations allow us to obtain microcosmic information such as the

phonon spectrum, phonon scattering, infrared spectrum, and Raman spectrum. This helps to deeply understand the physical essence of κ_l and reveal the relationship between material structure and thermal transport properties [24–27].

DFT is now routinely used to map the structural, mechanical, electronic, thermal, vibrational, and optical properties of solids [28–30]. For the MAB-phase Cr_4AlB_4, such an extensive set of properties has already been evaluated from the first-principles methods. The computed data closely match experimental results and confirm both the mechanical and dynamic stability of Cr_4AlB_4. High-throughput calculations and machine learning are now pivotal in fast-tracking MAB-phase discovery. For example, through machine learning screening, 47 stable hexagonal MBene materials were successfully identified from 15771 candidate materials. This data-driven approach has greatly improved the efficiency of new material discovery [31, 32].

Thermal conductivity (κ_l) is investigated by combining DFT with non-equilibrium molecular dynamics (NEMD) simulations. For example, researchers identified spinel oxides with low thermal conductivity and low thermal expansion coefficient by fitting DFT calculation data with machine learning potentials [33]. To assess κ_l of MAB phases, a new approach combines density-functional perturbation theory with the Boltzmann transport equation. This method can reveal the phonon scattering mechanism at the atomic scale and provide theoretical guidance for material design. To overcome the problems of long cycle and large amount of calculations in traditional DFT calculations, high-throughput computation combined with machine learning (ML) has become an important strategy to accelerate the discovery of the new MAB-phase materials. Li et al. [34] conducted high-throughput DFT calculations on M_2AX and M_2AB_2 phases and combined them with machine learning methods to successfully identify the 'fingerprint' characteristics of materials with excellent low κ_l. Using moment tensor potentials (MTPs) trained and validated against first-principles data, He et al. [35] computed κ_l of $La_2Zr_2O_7$, $La_2SrAl_2O_7$ and $LaPO_4$ by solving the linearized Boltzmann equation with three- and four-phonon scattering and by using Kubo–Green equilibrium molecular dynamics. The same MTP-driven framework accurately captures higher-order phonon processes and offers a powerful route to quantify anharmonicity and its impact on thermal transport in MAB phases. Advances in computational materials science and high-throughput techniques now allow the structure, stability, and full property suite of MAB phases to be predicted from the first-principles methods, compressing discovery and characterization cycles from years to hours [36].

In 2024, Lu et al. [37] conducted a systematic study on the lattice dynamics, Raman, and infrared (IR) vibrations of 24 stable Al/Si-containing MAB phase materials using DFT. Beyond computing the Raman spectral signatures, they recorded experimental spectra for Cr_2AlB_2 and Mo_2AlB_2. They found that the predicted peaks deviated from the measured ones by $< 1.9\%$ on average — compelling evidence that first-principles modelling reliably captures the Raman response of MAB phases. Wei et al. [38] calibrated the Raman and fluorescence spectra of fluorescent pressure sensors such as ruby, Sm^{2+}:SrB_4O_7 and Sm^{3+}:YAG (YAG stands for yttrium aluminum garnet). The calibration took into account the influence of temperature on spectral lines, which indirectly demonstrates the potential of Raman spectroscopy in temperature monitoring and thermal property research.

Progress on MAB-phase thermal conductivity is undoubtedly emerging. Jiang et al. [39] used first-principles calculations to map the structural stability, elastic constants and hardness of Cr–Al–B ternaries, laying the groundwork for future thermal transport studies. Four compounds, including Cr_3AlB_4, were found to have stable crystal structures, which provides a basis for further research on their lattice thermal conductivity and other properties. Tugbey et al. [40] studied the electron–phonon coupling and thermal conductivity properties of ternary borides such as MoAlB, WAlB, Tc_2AlB_2, and Cr_2AlB_2. Thermal conductivity values calculated by various methods are basically consistent, verifing the reliability of these methods. At 300 K, the lattice thermal conductivity κ_l of the MoAlB lattice along different directions are 27 W/(m K) (x direction), 16 W/(m K) (y direction), and 30 W/(m K) (z direction). Li et al. [41] studied the electronic, optical and thermal behaviour of Cr_3AlB_4, reporting a thermal expansion coefficient of 1.8×10^{-5} K^{-1} at 300 K and 0 GPa — higher than that of typical MAX phases. The authors noted that strong reflectivity across the IR, visible and ultraviolet (UV) ranges could make the compound attractive for optical coatings and mirrors.

The discovery of the crystal structure in Cr_4AlB_4 further expanded the members of the MAB phase family and promoted in-depth research on their physical and chemical properties [36, 42]. Raman spectroscopy, a key non-destructive probe, is routinely applied to examine phonon modes, crystal symmetry, defects, and doping in MAB phases [43–45]. For example, in the study of the electronic structure of a single crystal $YCrB_4$ from MAB phase family, microfocused photoelectron spectroscopy was used to reveal the three-dimensional band structure of this crystal. The results are highly consistent with the band dispersion calculated by the first-principles methods, confirming that it is a topologically trivial narrow-bandgap insulator [46]. High-throughput computing methods have been used to predict Raman spectra to overcome the time-consuming problem of traditional DFT calculations. This method can help

researchers obtain reference Raman spectra from first-principles calculations, thereby explaining better experimental data [45].

As a typical MAB phase material, Cr_3AlB_4 has attracted widespread attention in the field of advanced materials due to its unique layered crystal structure and excellent properties combining both metallic and ceramic characteristics. Research on Cr_3AlB_4 is currently in an active stage of interdisciplinary integration. By combining advanced theoretical calculations, high-throughput screening, machine learning, and experimental characterization (e.g. Raman spectroscopy), researchers are striving to fully understand the structure of the crystal, phonon dynamics, and thermal transport mechanisms, with the aim of providing new material solutions for innovative applications in aerospace, energy, electronics, and other fields. Understanding the thermal conductivity of MAB phase materials such as Cr_3AlB_4 is crucial for evaluating their potential as thermoelectric or thermal barrier materials. However, current research on MAB phase materials mainly focuses on synthesis, structural characterization, and basic performance testing, while research on their lattice thermal conductivity is relatively limited. Most existing studies focus on MAX phase materials or other similar layered compounds, and there is currently no systematic first-principles simulation study on the thermal conductivity of Cr_3AlB_4 — a specific ternary layered boride. Therefore, conducting aforementioned study by us will help fill the gap and enrich and improve the theory of thermal transport in MAB phase materials [47–52].

2. Methods

The calculations in this study are based on DFT using the Vienna *Ab initio* Simulation Package (VASP). During the computational process, the Perdew–Burke–Ernzerhof (PBE) functional, in combination with the generalized gradient approximation (GGA) method, is used to calculate the exchange–correlation energy. The plane wave cutoff energy is set to 700 eV to ensure the required accuracy of the calculations. The energy convergence of 1×10^{-8} eV and a force convergence of 1×10^{-7} eV/Å were chosen, and a grid of $11 \times 11 \times 11$ k-points was selected for sampling the Brillouin zone in this study [53–56].

To characterize the spectrum of the Cr_3AlB_4 material, accurate calculations of the infrared and Raman specta were achieved using Phonopy software, DFPT (density functional perturbation theory) method, and Phonopy-Spectroscopy software [57]. Calculations of thermal and phonon-related properties were performed using a combination of VASP and ShengBTE software. To analyze the force constants (IFCs) between harmonic and anharmonic

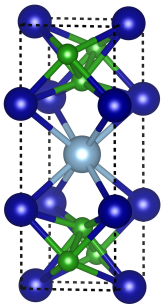

Fig. 1. Diagram structure of Cr_3AlB_4.

atoms, a $2 \times 2 \times 2$ supercell generated by Phonopy software was used. The third-order force constants were computed considering third-order interactions, including an interaction up to the 13th nearest neighbour to ensure convergence. The resulting constants were entered into the ShengBTE package, where the Boltzmann equation for phonons was solved on the q-grid $30 \times 30 \times 30$ to obtain the lattice thermal conductivity and related transport data [58].

3. Results and discussion

3.1. Crystal structure

As shown in Fig. 1, Cr_3AlB_4 is a ternary-layered boride MAB phase ceramic composed of chromium (Cr, in blue), aluminum (Al, in bright gray), and boron (B, in green). It belongs to the orthorhombic system with space group Pmmm (no. 47). Cr_3AlB_4 has a layered structure, consisting of alternating Cr–B layers and Al atomic layers. Inter-layer bonding governs the mechanics, charge transport, and heat conduction. The Cr and B atoms in the Cr–B layer are bonded together by strong covalent bonds, forming a stable structural unit, while the Al atom layer is interspersed between the Cr–B layers. The presence of this strong covalent bond (between the Cr and B atoms) provides the Cr–B layer high stability and strength, enabling it to withstand certain external forces and temperature fluctuations. In contrast, the bond strength between the Al and Cr atoms is relatively weak, resulting in a diminished bonding force between the layers. Consequently, under specific conditions, it is easier for the layers to slip or peel apart.

4. Electronic band structure

The total energy is shown to determine convergence with increasing density of the Γ-centered k-grid, as illustrated in Fig. 2a. The horizontal dashed line indicates an accuracy of 1 meV per

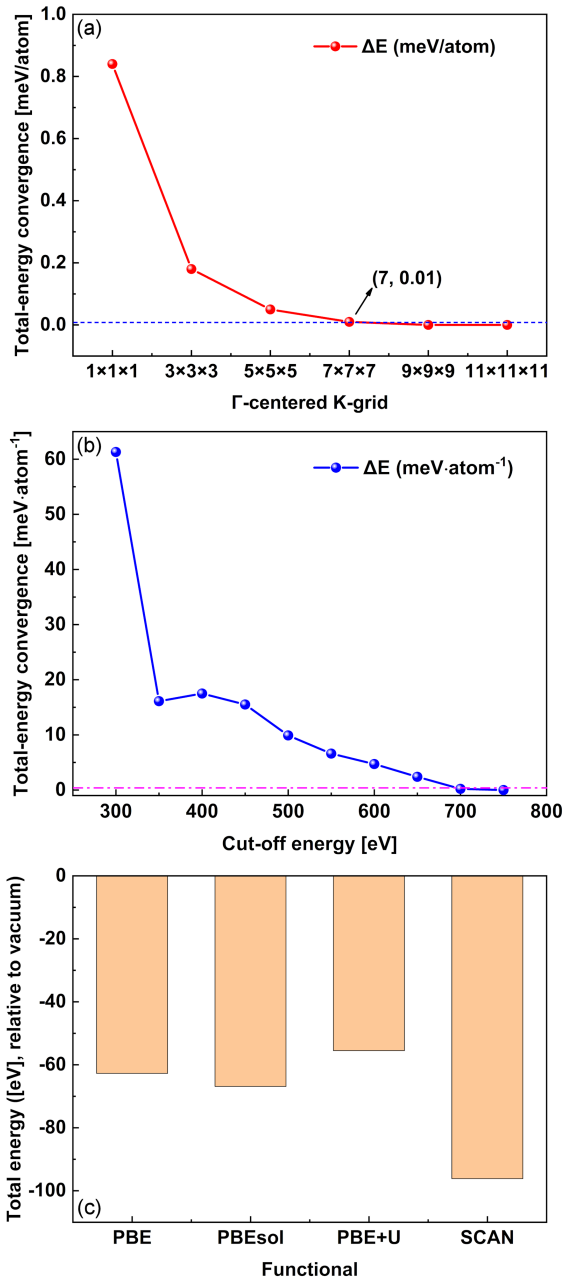

Fig. 2. Convergence of total-energy depending on (a) k-grid density, (b) energy cutoff, (c) PBE, PBEsol PBE+U and SCAN functionals.

atom. The k-grid densities used were: $1 \times 1 \times 1$, $3 \times 3 \times 3$, $5 \times 5 \times 5$, $7 \times 7 \times 7$, $9 \times 9 \times 9$ and $11 \times 11 \times 11$. As shown, the k-spacing is approximately 0.025 Å^{-1}, with the relative energy difference expressed in meV. This confirms that the adopted $11 \times 11 \times 11$ k-point grid is converged.

As shown in Fig. 2b, using a k-grid of $11 \times 11 \times 11$ the total energy convergence within 1 meV per atom was achieved at an cut-off energy E_{cut} of 650 eV. A value of 700 eV (k-spacing ≈ 0.025 Å^{-1}) was chosen to ensure numerical robustness and compatibility with future higher-cutoff tests.

As can be seen in Fig. 2c, the PBE, PBEsol, PBE+U, and SCAN functionals were compared in benchmark tests. The difference in the calculated lattice constants is less than 0.4%, and the relative error in the obtained energy is below 25 meV per atom, which demonstrates that the qualitative trends reported in the paper remain unchanged. Although the absolute total energies differ by up to 34 eV, the relative energy differences and phonon trends are within 70 meV per atom and 5 cm^{-1}, respectively, as confirmed by the benchmark calculations on the parent Cr_3AlB_4 phase in Fig. 2c. Therefore, we adopted the PBE functional as the best compromise between numerical efficiency and acceptable accuracy in high-throughput trend prediction in compositional space. To maintain self-consistency in terms of structural, vibrational, and thermal properties, all calculations — including total energies, phonon spectra, Raman intensities, and lattice thermal conductivity — were performed using the PBE functional with the same converged basis set (700 eV, $11 \times 11 \times 11$). Consequently, the relative trends are unaffected by systematic exchange–correlation errors.

At last, we hypothesize that the choice of different parameters does not significantly affect the results obtained. Within the converged basis set ($11 \times 11 \times 11$, 700 eV), by varying the k-grid density, it turns out the choise of either E_{cutt} (650–750 eV) or the exchange–correlation functional (PBE, PBEsol, PBE+U, SCAN) will change the absolute total energies by up to 34 eV. However, the relative energy differences and structural/phonon trends remain below 70 meV per atom and 0.4%, respectively. Therefore, the qualitative conclusions reported in the paper are robust to parameter choice.

The characteristics of the electronic band structure of a material are closely related to its layered crystal structure, chemical bonding properties, and electronic configuration. The valence electron configurations of Cr, Al, and B are $3d^5 4s^1$, $3s^2 3p^1$, and $2s^2 2p^1$, respectively. As illustrated in Fig. 3a, Cr_3AlB_4 is a representative member of the MAB phase family. Cr_3AlB_4 displays conduction and valence bands that intersect the Fermi level, which indicates metallic behavior of Cr_3AlB_4. As shown in Fig. 3b, this characteristic arises from the synergistic effect of the $3d$ electrons of Cr and the strong covalent bonds formed by the $2p$ electrons of B, along with the weaker metallic bonds between the layers. The crystal structure of Cr_3AlB_4 consists of alternating layers of Cr–B and Al atoms. The strong covalent bond is formed within the Cr–B layer due to the hybridization of the d orbitals of Cr and the p orbitals of B. The Al atomic layer is combined with the Cr–B layer through weaker metallic bonds, resulting in reduced band dispersion along the c-axis direction. There is significant hybridization between the $3d$ orbitals of Cr and the $2p$ orbitals of B near the Fermi level. This

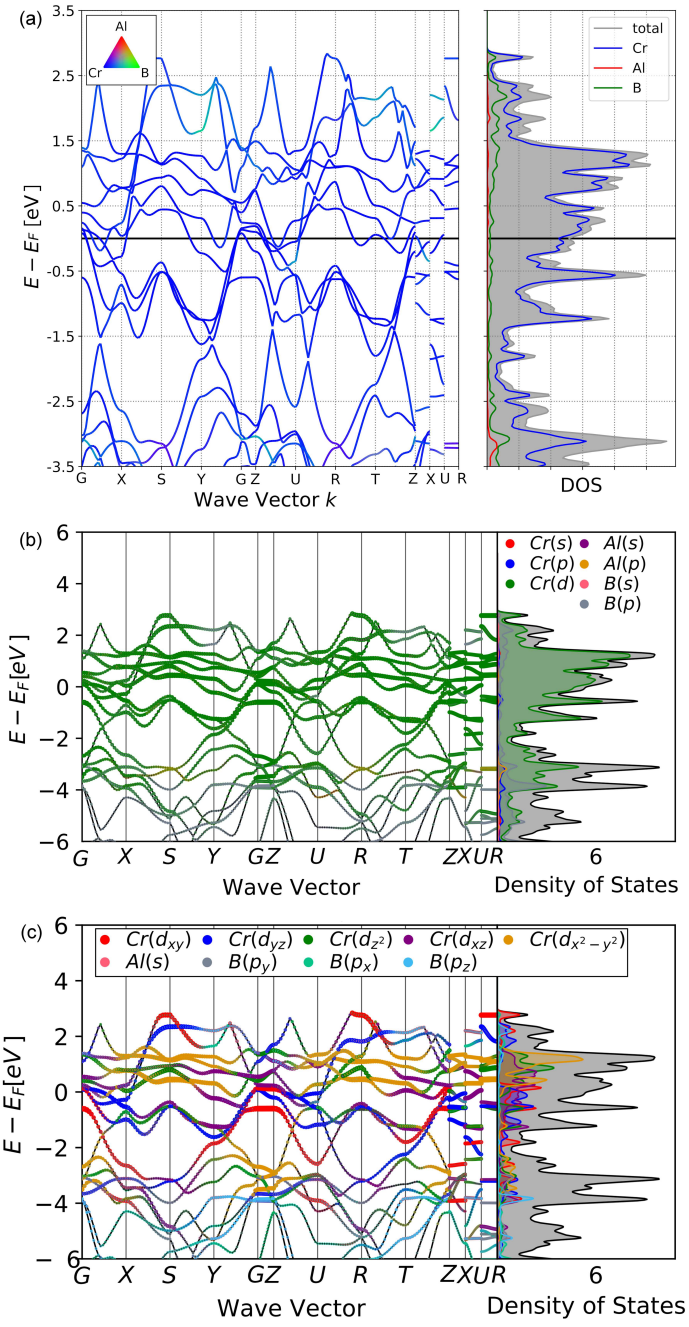

Fig. 3. Electronic structure of Cr_3AlB_4: (a) band structure and projected density of states, (b) element-projected band structure and element-projected DOS, (c) orbital-projected band structure and orbital-projected DOS.

interaction results in band crossing at the Fermi surface, facilitating the formation of metallic conductivity. The minimum conduction band and maximum valence band of Cr_3AlB_4 may partially overlap, allowing electrons to contribute to conduction without requiring a transition. This behavior is consistent with the characteristics of metals.

Further, as shown in Fig. 3c, the d orbital of Cr is dominant. Near the Fermi level, the $3d$ orbitals of Cr (including d_{xy}, d_{yz}, d_{zx}, and d_{x2-y2}) contribute significantly to the density of states (DOS). These orbitals are hybridized with the $2p$ orbitals of B to create bonding and anti-bonding states. The anti-bonding state can lead to a high density of states region near the Fermi level, which enhances the metallicity of the material. At the same time, the Cr^{3+} ion has a $3d^3$ electron configuration. In the octahedral coordination field, the $3d$ orbitals are split into the t_{2g} orbitals (i.e., d_{xy}, d_{yz}, d_{xz}), which represent the lower-energy state, and the e_g orbitals (i.e., d_{x2-y2}, d_{z2}), which represent the higher-energy state.

4.1. Phonon dispersion

The phonon dispersion of Cr_3AlB_4 in Fig. 4 does not show any imaginary branches, confirming the dynamic stability of this material. Low-lying modes are dominated by Cr displacements, with a smaller contribution from Al. These modes correspond to interlayer shearing and bending and contribute most to thermal conductivity. The mid- and high-frequency bands arise primarily from the motions of B atoms combined with Al and Cr atoms, particularly involving the coupled Al–B vibrations. Optic branches above ≈ 13 THz — localized B–B covalent oscillations — scatter strongly and carry little heat because their short mean free paths limit their contribution to thermal conductivity κ_l.

4.2. Raman spectrum

In this study, the infrared (IR) and Raman spectrum of Cr_3AlB_4 are analyzed, focusing solely on the phonon frequency at the center of the Brillouin zone (i.e., at Γ point, indicated as 'G' in the figures). The VASP program can directly calculate the phonon frequency at the Γ point using either the finite displacement method or the linear response method. The phonon frequencies and eigenvectors are obtained within the harmonic approximation using density functional perturbation theory (DFPT) by evaluating the second-order force-constant matrix. The IR intensity of any mode is then given by the square of the dot product between the mode's eigenvector and the Born effective charge tensor. Thus,

$$I_{\mathrm{IR}}(s) = \sum_{\alpha} \left| \sum_{j} \sum_{\beta} Z^{*}_{\alpha\beta} X_{\beta}(s,j) \right|^{2}. \tag{1}$$

Here, $X_\beta(s,j)$ is the normalized vibrational eigenvector of the j-th phonon mode for the s-th atom in the unit cell. Raman activity tensors for each eigenmode are obtained by numerically differentiating the high-frequency dielectric constant ε^{∞} with respect to the normal-mode amplitude $Q(s)$ via a central-difference scheme. Phonopy and Phonopy-Spectroscopy software were employed to compute the phonon frequency and the corresponding Raman intensity, finally expressed as

$$I_{\mathrm{Raman}} = 45 \left| \frac{1}{3}(I_{11}+I_{22}+I_{33}) \right|^{2} + \frac{7}{2}\Big[(I_{11}-I_{22})^{2} + (I_{11}-I_{33})^{2} + (I_{22}-I_{33})^{2} + 6\left(I_{12}^{2}+I_{13}^{2}+I_{23}^{2}\right) \Big]. \tag{2}$$

Cr_3AlB_4 has 24 zone-center phonons; at the Γ point, they decompose into irreducible representations in the following way

$$\mathrm{M} = 3\mathrm{A}_g + 5\mathrm{B}_{1u} + 3\mathrm{B}_{2g} + 5\mathrm{B}_{2u} + 3\mathrm{B}_{3g} + 5\mathrm{B}_{3u}. \tag{3}$$

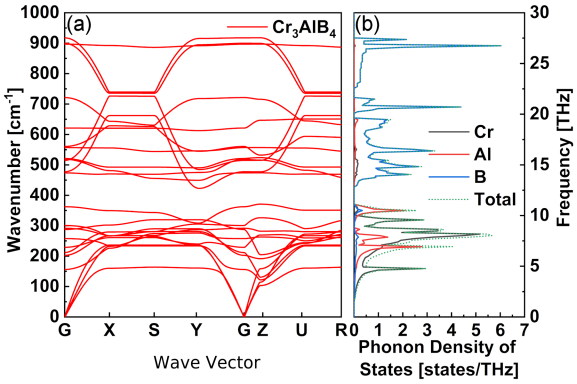

Fig. 4. (a) Phonon dispersion and (b) projected phonon density of states (PhDOS) of Cr_3AlB_4.

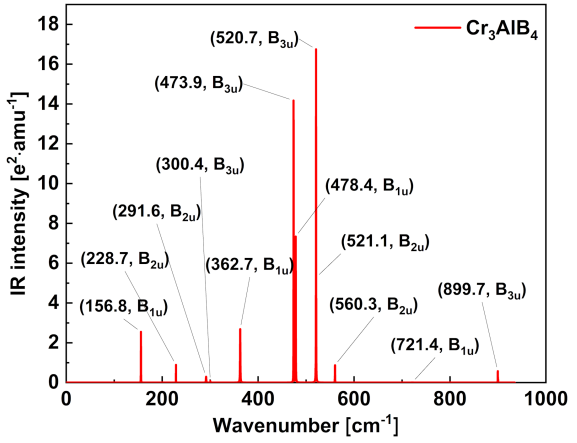

Fig. 5. Infrared spectrum of Cr_3AlB_4.

The acoustic branch has three irreducible representations, corresponding to 3 lattice waves, which can be given as follows

$$\Gamma_{\mathrm{acoustic}} = \mathrm{B}_{1u} + \mathrm{B}_{2u} + \mathrm{B}_{3u}. \tag{4}$$

The optical branch consists of 21 irreducible representations, corresponding to 21 lattice waves, which can be given as follows

$$\Gamma_{\mathrm{optic}} = 3\mathrm{A}_g + 4\mathrm{B}_{1u} + 3\mathrm{B}_{2g} + 4\mathrm{B}_{2u} + 3\mathrm{B}_{3g} + 4\mathrm{B}_{3u}. \tag{5}$$

The lettered table indicates 12 infrared-active optical modes ($4\mathrm{B}_{1u} + 4\mathrm{B}_{2u} + 4\mathrm{B}_{3u}$) and 9 Raman-active modes ($3\mathrm{A}_g + 3\mathrm{B}_{2g} + 3\mathrm{B}_{3g}$) for Cr_3AlB_4. The computed spectrum, obtained after structural relaxation, is shown in Figs. 5 and 6.

Figure 5 shows the peak positions and vibration intensities of twelve IR vibration modes of the Cr_3AlB_4 material. The modes at 473.9 cm^{-1} (B_{3u}), 478.4 cm^{-1} (B_{1u}), and 520.7 cm^{-1} (B_{3u}) exhibit strong IR vibrational intensity. On the other hand, the IR vibrational intensities of the modes at 156.8 cm^{-1} (B_{1u}), 228.7 cm^{-1} (B_{2u}), 362.7 cm^{-1} (B_{1u}), 560.3 cm^{-1} (B_{2u}), and 899.7 cm^{-1} (B_{3u}) are low but can be easily identified. The IR vibrational intensities of the modes at 291.6 cm^{-1} (B_{2u})

and 300.4 cm^{-1} (B_{3u}) are very low and thus require careful identification for confirmation. The IR vibration intensity at 721.4 cm^{-1} (B_{1u}) is too low to be detected. The IR peak corresponding to the 521.1 cm^{-1} (B_{2u}) mode is very close to the peak at 520.7 cm^{-1} (B_{3u}), making them nearly indistinguishable. Structurally, Cr_3AlB_4 exhibits a layered architecture, alternating between metal layers (Cr/Al) and B layers. The boron atoms form a chain structure. Low-frequency IR modes arise from interlayer shearing and out-of-plane motions of the Cr and Al planes, governed by covalent–metallic bonding. On the other hand, the contributions of Al and B atomic vibrations at mid- and high-frequency level are significant. This is due to weak interactions in the metal-boron systems, such as transverse vibrations of Cr–B and Cr–Al, as well as in-plane bending and twisting vibrations of the B chains. High-frequency modes primarily arise from the motion of boron atoms, driven by strong covalent stretching of the B–B bonds.

As shown in Fig. 6, Cr_3AlB_4 exhibits nine Raman-active modes: 155.8 cm^{-1} (B_{2g}), 202.4 cm^{-1} (B_{3g}), 287.5 cm^{-1} (A_g), 473.9 cm^{-1} (B_{2g}), 520.3 cm^{-1} (B_{3g}), 521.1 cm^{-1} (B_{2g}), 556.9 cm^{-1} (B_{3g}), 620.8 cm^{-1} (A_g), and 896.7 cm^{-1} (A_g). Among these Raman vibrational modes, all modes are easily distinguishable, except for the 520.3 cm^{-1} (B_{3g}) mode, as it is too close to the 521.1 cm^{-1} (B_{2g}) mode. Overall, the Raman spectrum closely resembles the IR spectrum. The reduced frequencies reflect both the larger masses of Cr and Al and the ease with which the relatively soft Cr–Al bonds distort during bending. The intermediate frequency may result from the interaction between the metal layer and the B layer, or from in-plane bending or twisting vibrations of the B–B chain. The elevated frequencies arise from the stiff covalent B–B interactions, with Cr and Al contributing minimal motion. The combination of the strong Cr–B bonding and the low mass of boron shifts the stretching modes to higher frequencies. This trend is reflected in the phonon dispersion and the projected DOS shown in Fig. 4.

4.3. Lattice thermal conductivity

In general, thermal conductivity increases with longer phonon relaxation times (i.e., lower scattering rates) and higher group velocities, while it decreases as the Grüneisen parameter, available phase space, number of scattering channels, or overall scattering rate increase. Through the ShengBTE software package, an accurate solution for the lattice thermal conductivity of the material can be obtained. The lattice thermal conductivity, denoted as κ_l, is calculated as follows

$$\kappa_l = \frac{1}{N V k_B T^2} \sum_{\lambda} f_0 \left(f_0+1\right) \left(\hbar\omega_\lambda\right)^2 \left(v_\lambda^z\right)^2 \tau_\lambda. \quad (6)$$

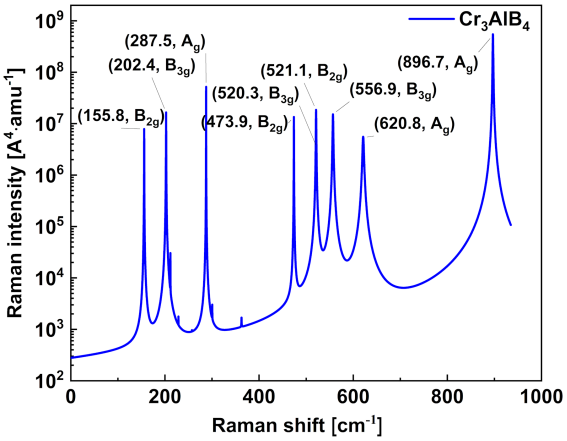

Fig. 6. Raman spectrum of Cr_3AlB_4.

Here, $\boldsymbol{v}_\lambda$ is the phonon group velocity, τ_λ is the relaxation time (the inverse of the scattering rate), and $(1/\tau_\lambda)$ accounts for isotopically disordered anharmonic processes with two and three phonons. The available phase-space volume is quantified by

$$W_\lambda^{\pm} = \sum_{\lambda'\lambda''} \left[\frac{\left(f^0_{\lambda'} + \frac{1}{2}\right) \mp \left(f^0_{\lambda''} + \frac{1}{2}\right)}{\omega_\lambda \omega_{\lambda'} \omega_{\lambda''}} \right] \delta\left(\omega_\lambda \pm \omega_{\lambda'} - \omega_{\lambda''}\right). \quad (7)$$

Ultimately, the anharmonic three-phonon rate $(1/\tau_\lambda^{\mathrm{ph}})$ is governed by the weighted phase space $(W_\lambda^{\pm})$ and the Grüneisen parameter (γ); together with the group velocity $(\boldsymbol{v}_\lambda)$ and relaxation time (τ_λ) they determine the lattice thermal conductivity [59, 60].

4.3.1. Cumulative lattice thermal conductivity

Figure 7 shows the cumulative lattice thermal conductivity of Cr_3AlB_4 as a function of the phonon mean free path (MFP) at 300 K. The curve stabilizes above a value of 278.3 nm, revealing that only phonons travelling a distance shorter than this critical value contribute to κ_l. Once the grain size surpasses 278.3 nm, the thermal conductivity of Cr_3AlB_4 stabilizes because long-MFP phonons no longer feel boundary to the scattering; the converged bulk value is 87.9 W/(m K).

A careful inspection of the phonon dispersion in Fig. 4 shows that the vibrations of Cr and a minority of Al atoms are confined to the lowest-frequency longitudinal acoustic (LA) branches. In the range from 0 and 5.1 THz, Cr atoms dominate the vibrational spectrum. From 5.7 to 8.9 THz, the coupled Cr–Al motion governs the lattice dynamics, whereas the branches flatten out between 8.9 and 10.0 THz. In the range 10.0–11.3 THz, the motion is a three-component mixture, but in it the Al

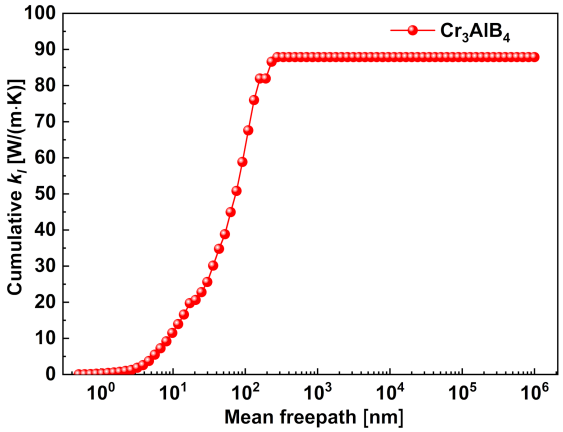

Fig. 7. Cumulative lattice thermal conductivity as a function of the phonon mean free path of Cr_3AlB_4.

displacements carry the largest weight. Flat optical branches appear between 12.8 and 27.7 THz, producing pronounced peaks in the phonon density of states. These high-frequency optical branches are primarily composed of B atoms, with trace amounts of Cr and Al atoms. A 1.5-THz gap separates the lowest optic branch from the acoustic manifold. This gap is largely attributed to the contributions of Al and B atoms in the Cr_3AlB_4 material. The slight difference in atomic mass between Al and B facilitates phonon energy exchange and heat transfer, which may contribute to the high κ_l value of Cr_3AlB_4. Phonon dispersion in Cr_3AlB_4 is relatively discrete; it occurs in the ranges: 0–5.1 THz, 8.9–10.0 THz, and 10.0–11.3 THz. Hybridization between Cr and Al is minimal, which may result in a reduced phase space. More numerous and stronger scattering channels intensify phonon collisions, producing a markedly higher relative intensity.

4.3.2. Relaxation time

Phonon lifetime is set by the cumulative effect of umklapp, boundary and defect scattering; stronger anharmonicity boosts phonon–phonon coupling and lowers the value of κ_l. ShengBTE software allows for estimation of the total rate (isotope and three-phonon anharmonic), the inverse of which gives τ. Figure 8 displays the frequency-dependent phonon lifetime in Cr_3AlB_4 at 300 K. Acoustic and low-lying optic modes share comparably long τ at low frequency, although the acoustic set dominates: $TA_1 \leq 98$ ps, $TA_2 \leq 84$ ps, while LA remains shorter, i.e., ≤ 46 ps (as a reminder, TA — transverse acustic, LA — longitunal acustic). Between 4.3 and 27.5 THz the spectrum is governed by optic branches whose lifetimes are uniformly lower than 83 ps. Between 4.3 and 8.2 THz the lifetimes overlap those of the TA_1, TA_2 and LA branches;

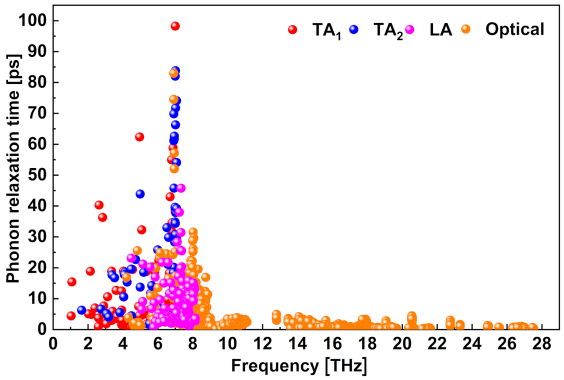

Fig. 8. Phonon relaxation time of Cr_3AlB_4.

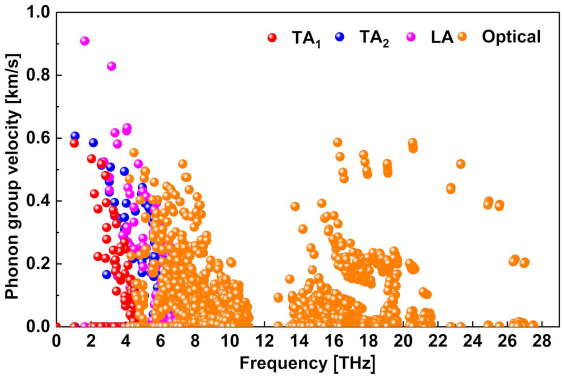

Fig. 9. Phonon group velocity of Cr_3AlB_4.

at 300 K all these low-lying modes, i.e., acoustic and optic alike, possess extended τ, suppressing scattering in the low-frequency window. The extended lifetimes indicate that phonons are efficient heat carriers, underpinning the comparatively high κ_l value of Cr_3AlB_4. In the optic mode of the 7.5–20 THz window, τ spans 0–32 ps, so even though these branches contribute, the dominant contribution to κ_l still comes from the acoustic and lowest-frequency optic modes.

4.3.3. Group velocity

Phonon group velocity v_λ, defined as the slope of the dispersion $\partial\omega/\partial q$, is a key metric for heat-transport efficiency and is obtained directly from the gradient of the phonon branches [61]. Figure 9 reveals modest group velocities throughout Cr_3AlB_4. The acoustic triad (TA_1, TA_2, LA) clusters near 3.2 THz and overlaps with optic velocities; the TA_1 mode is the slowest, peaking at ≈ 0.58 km/s, while LA reaches ≈ 0.91 km/s and $TA_2 \approx 0.61$ km/s. Strikingly, optic modes around 7 THz fall below acoustic values at a velocity of ≈ 0.55 km/s, while high-frequency optic velocities (12.8–27.5 THz) rise slightly to ≈ 0.59 km/s. The low group velocity stems mainly from the soft Cr–Al

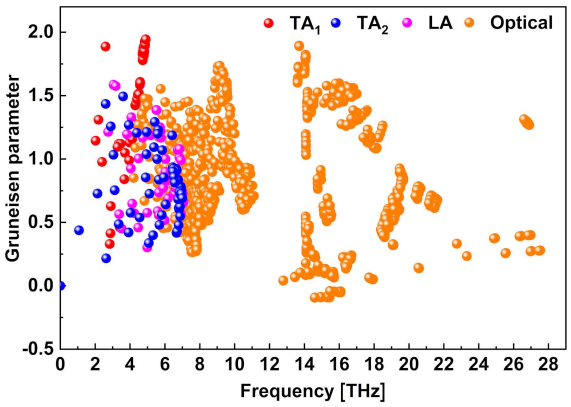

Fig. 10. Grüneisen parameter of Cr_3AlB_4.

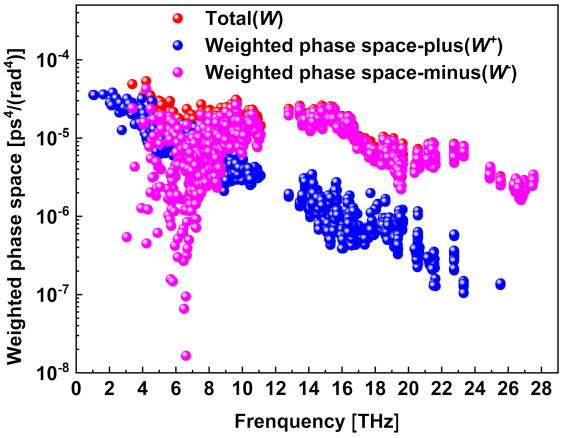

Fig. 11. Weighted three-phonon phase space of Cr_3AlB_4.

and Al–B bonds together with the large average atomic mass. Yet it does not predetermine a low κ_l because the lattice thermal conduction is governed by several competing factors.

4.3.4. Grüneisen parameter

Figure 10 shows that, across both acoustic and optical branches, Cr_3AlB_4 displays a uniformly small $|\gamma|$ for every phonon mode. Cr_3AlB_4 exhibits a frequency near 5 THz, with an absolute value of γ approximately equal to 1.94, which is characteristic of the TA_1 mode. By comparison, the TA_2 and LA branches exhibit even smaller $|\gamma|$, peaking at 1.49 and 1.59, respectively, while throughout the 4.21–27.5 THz optical window $|\gamma|$ stays below 1.89. From the results, the $|\gamma|$ for Cr_3AlB_4 is low, indicating that the anharmonic effects within the crystal are weak. This suggests that the phonon–phonon interactions are relatively minor, which reduces the probability of phonon scattering during propagation. Consequently, the weak anharmonicity lets phonons propagate heat efficiently, raising κ_l. Moreover, the negative γ values hint at possible negative thermal expansion in Cr_3AlB_4.

4.3.5. Weighted phase space

The abundance of scattering channels — that is, the availability of phonon triplets that satisfy the conservation of energy and momentum — is quantified by the weighted phase space defined in (7). The anharmonic three-phonon scattering rate is derived from the sum of all three-phonon transition probabilities and is dependent on the weighted phase space. The weighted phase space is described by two channels, namely the absorption process (W_λ^+, two phonons merging into one) and the emission process (W_λ^-, one phonon splitting into two).

As shown in Fig. 11, in the frequency range of 1–4.6 THz the obtained values of W_λ^+ of Cr_3AlB_4 are significantly high, with notable peaks at 2.2 THz and 3.0 THz. In the ranges 4.2–7.6 THz and 12.8–27.5 THz, the W_λ^- values of Cr_3AlB_4 increase rapidly, reaching higher values with peaks observed at 4.2 THz, 9.7 THz, 15.4 THz, and beyond. A distinct gap in the results appears for frequencies between 11.1 THz and 12.8 THz. This is a phase space region with high scattering ability, corresponding to optical branching regions characterized by the presence of Al and a minimal amount of B. This highlights the importance of these optical branches in facilitating phase-space scattering and reducing thermal conductivity. Cr_3AlB_4 also displays a reduced weighted phase space W_λ, reflecting weaker anharmonic scattering and hence increased lattice thermal conductivity.

In general, the crystal structure of Cr_3AlB_4 is characterized by high-density atomic packing, short atomic bond distances, and strong covalent and metallic bonding. The compact structure directly results in short bond lengths (such as Cr–Al, Cr–B, and Al–B bonds) and high bond energies. The lattice rigidity is significant, and the dense arrangement restricts the amplitude of atomic thermal vibrations, thereby reducing the effects of anharmonic vibrations. Acoustic phonons in Cr_3AlB_4 are barely scattered by point defects or isotopes, a feature that can sustain high κ_l. In Cr_3AlB_4, the difference between the strong covalent bonding and the light B mass is modest. In Cr_3AlB_4, strong covalent bonding suppresses anharmonic effects. The light mass of B contributes minimally to anharmonicity. The robust bond strength-particularly the metal-covalent mixed B–Cr bond-provides a strong elastic restoring force and high phonon group velocities.

The tightly packed, high-symmetry structure of Cr_3AlB_4 generates strong covalent interactions that reinforce low-frequency acoustic branches. This arrangement sharply contracts the weighted phase

space, suppresses phonon scattering, and thereby postpones the shortening of τ caused by phonon–phonon interactions. At the same time, the amplitude of atomic vibrations in the compact structure is small, and the phonon frequency is relatively insensitive to volume perturbations. Additionally, the effective range of anharmonic interactions is limited. The absolute value of the Grüneisen parameter γ is small, which directly increases the value of κ_l. Analyzing the performance of Cr_3AlB_4 material in infrared and Raman spectroscopy, one can obtain characteristics that are closely related to lattice vibration properties (phonon behavior).

These traits also highlight how heat conduction in Cr_3AlB_4 is shaped by the interplay between phonon transmission efficiency, scattering channels, and underlying lattice dynamics. Cr_3AlB_4 shows only feeble infrared absorption at low frequencies. This indicates that the absorption intensities at 156.8 cm^{-1} (B_{1u}), 228.7 cm^{-1} (B_{2u}), 291.6 cm^{-1} (B_{2u}), 300.4 cm^{-1} (B_{3u}), and 362.7 cm^{-1} (B_{1u}) in the low-frequency region of Cr_3AlB_4 are low. This may be attributed to the relatively simple and orderly lattice vibration modes within the material, which results in reduced phonon scattering. This characteristic is favorable for heat conduction and corresponds to the higher κ. The Raman spectrum of the Cr_3AlB_4 material exhibits distinct low-frequency phonon peaks at 155.8 cm^{-1} (B_{2g}), 202.4 cm^{-1} (B_{3g}), and 287.5 cm^{-1} (A_g). These sharp peaks indicate that phonons experience less scattering during propagating through the Cr_3AlB_4 lattice, which improves heat conduction and contributes to the higher κ. The low-frequency phonon mode is closely associated with the long-range order and thermal conductivity of the lattice. Cr_3AlB_4 exhibits pronounced phonon peaks in the low-frequency region, indicating that the lattice structure of the Cr_3AlB_4 material is relatively intact. This results in minimal phonon propagation resistance, which facilitates efficient heat conduction.

The structural characteristics of Cr_3AlB_4 suggest its potential application in high-temperature thermal management, heat dissipation in electronic devices, and other fields. This paper provides a theoretical foundation for understanding the high thermal conductivity of Cr_3AlB_4. Refinement of the growth protocol will further improve the crystal quality and thermal conductivity, positioning the material for competitive deployment in nuclear and aerospace technologies.

5. Conclusions

Using first-principles calculations, this study determined the Raman spectrum and lattice thermal conductivity of Cr_3AlB_4; at the Brillouin-zone center the compound possesses 9 Raman-active and 12 IR-active modes. Results for the Cr_3AlB_4 material showed that κ_l = 87.9 W/(m K) when the MFP exceeds 278.3 nm. At 300 K, the relaxation time of various phonons in Cr_3AlB_4 is significant. Weak mutual scattering among low-frequency phonons allows acoustic modes and the lowest-lying optic modes to make the dominant contribution to thermal conduction process. Despite the intrinsically low phonon group velocities, κ_l remains high. The absolute value of the Grüneisen parameter γ is small, which is beneficial for increasing thermal conductivity. Additionally, γ is negative, suggesting the possibility of negative thermal expansion. The weighted phase space of Cr_3AlB_4 is limited, and the anharmonic scattering rate is low, resulting in an increased value of κ_l. This study provides a robust theoretical basis for the potential deployment of Cr_3AlB_4 in diverse technological fields.

Acknowledgments

The authors are grateful for the financial support provided by the Henan Provincial Science and Technology Research Project (Grant No. 252102230086) and the Interdisciplinary Science Project of Nanyang Institute of Technology (Grant No. 230072).

References

[1] C. Roy, S. Mondal, P. Banerjee, S. Bhattacharyya, *Adv. Powder Technol.* **34**, 103983 (2023).

[2] B. Demir, E. I. Duden, E. Ayas, *J. Alloy. Compd.* **953**, 170115 (2023).

[3] A.Y. Potanin, E.A. Bashkirov, A.Y. Karpenkov, E.A. Levashov, *Materialia* **33**, 101993 (2024).

[4] J. Słomiński, S. Komarek, D. Zientara, D. Madej, A. Gubernat, *Ceram. Int.* **49**, 30845 (2023).

[5] Q. Zhang, Y. Zhou, X. San, W. Li, Y. Bao, Q. Feng, S. Grasso, C. Hu, *J. Adv. Ceram.* **11**, 1764 (2022).

[6] A. Madhubala, S.G.K. Manikandan, R.U. Rani, M. Kamaraj, *J. Alloy. Compd.* **1007**, 176353 (2024).

[7] J.A. Mohammed Abdulwahed, *Acta Phys. Pol. A* **143**, 25 (2023).

[8] V. Sharma, R. Barua, *Materials* **17**, 3886 (2024).

[9] S. Mondal, C. Roy, S. Bhattacharyya, *Mater. Today Chem.* **37**, 102004 (2024).

[10] L. Benahmedi, A. Besbes, R. Djelti, *Acta Phys. Pol. A* **147**, 393 (2025).

[11] V. Natu, S.S. Kota, M.W. Barsoum, *J. Eur. Ceram. Soc.* **40**, 305 (2020).

[12] M. Fodil, O. Baraka, A. Mokadem, *Acta Phys. Pol. A* **146**, 143 (2024).

[13] B. Zhao, X. Wang, L. Yu, Y. Liu, X. Chen, B. Yang, G. Yang, S. Zhang, L. Gu, X. Liu, *Adv. Funct. Mater.* **32**, (2021).

[14] Z. Guo, X. Jiang, *J. Phys. Chem. Solids* **139**, 109330 (2020).

[15] Q. Liang, S. Dwaraknath, K.A. Persson, *Sci. Data* **6**, (2019).

[16] M.N. Popov, J. Spitaler, V.K. Veerapandiyan, E. Bousquet, J. Hlinka, M. Deluca, *Npj Comput. Mater.* **6**, (2020).

[17] S. Wang, L. Chen, H. Hao, C. Qiao, J. Song, C. Cui, B. Liu, *Sci. Rep.* **14**, 15030 (2024).

[18] S. Mandal, I. Maity, A. Das, M. Jain, P.K. Maiti, *Phys. Chem. Chem. Phys.* **24**, 13860 (2022).

[19] A.A. Yahaya, W.A. Yahya, A.S. Ahmed, A.A. Sholagberu, *Acta Phys. Pol. A* **145**, 194 (2024).

[20] B. Xu, Z. Shi, H. Yin, R. Zhang, *Solid State Commun.* **356**, 114971 (2022).

[21] S.O. Akande, B. Samanta, C. Sevik, D. Çakır, *Phys. Rev. Appl.* **20**, 044064 (2023).

[22] J. Tao, N. Arshad, G. Maqsood, M.S. Asghar, F. Zhu, L. Lin, M.S. Irshad, X. Wang, *Small* **20**, (2024).

[23] J.Y. Kim, H. Zhang, J. Xi, I. Szlufarska, *Chem. Mater.* **34**, 7807 (2022).

[24] X.-H. Li, C.-H. Xing, H.-L. Cui, R.-Z. Zhang, *J. Phys. Chem. Solids* **126**, 65 (2019).

[25] R. Wang, Y. Xiong, J. Sun, Y. Zhou, G. Song, G. Chen, X. Liu, *Appl. Phys. Lett.* **127**, 022202 (2025).

[26] H. Malekpour, A.A. Balandin, *J. Raman Spectrosc.* **49**, 106 (2017).

[27] A.S. Atalay, B. Derin, M.F. Khanghah, *Comput. Condens. Matter* **32**, e00731 (2022).

[28] S. Berri, N. Bouarissa, *Acta Phys. Pol. A* **146**, 270 (2024).

[29] S. Dahri, A. Jabar, L. Bahmad, L.B. Drissi, R.A. Laamara, *J. Mol. Graph. Model.* **139**, 109075 (2025).

[30] Q. Wei, Q. Wang, X. Xie, X. Jia, Z. Wu, H. Yan, M. Zhang, M. Hu, X. Zhu, *Acta Phys. Pol. A* **145**, 71 (2024).

[31] L. Zhichao, M. Dong, L. Xiongjun, Z. Lu, *Commun. Mater.* **5**, (2024).

[32] M. Matsubara, A. Suzumura, N. Ohba, R. Asahi, *Commun. Mater.* **1**, (2020).

[33] J. Liang, J. Liu, Y. Jing, H. Yang, S. Zhou, Y. Xia, F. Xu, L. Sun, P. Huang, *Materials Design* **255**, 114157 (2025).

[34] S. Li, Z. Yang, R. Khaledialidusti, S. Lin, J. Yu, M. Khazaei, J. Zhang, L. Sun, X. Li, W. Sun, *Acta Mater.* **254**, 119001 (2023).

[35] H. He, X. Wang, Y. Hao, C. Zeng, J. Li, H. Liu, Z. Gao, J. Feng, B. Xiao, *Comput. Mater. Sci.* **256**, 113954 (2025).

[36] M.M. Ali, M.A. Hadi, M.L. Rahman, F.H. Haque, A.F.M.Y. Haider, M. Aftabuzzaman, *J. Alloys Compd.* **821**, 153547 (2020).

[37] Z. Lu, X. Qi, X. He, J. Zhang, Y. Fan, H. Yin, G. Song, Y. Zheng, Y. Bai, *J. Am. Ceram. Soc.* **107**, 6853 (2024).

[38] Y. Wei, Q. Zhou, C. Zhang, L. Li, X. Li, F. Li, *J. Appl. Phys.* **135**, 105902 (2024).

[39] J. Wei, L. Zhang, Y. Liu, *Solid State Commun.* **326**, 114182 (2021).

[40] T. Kocabas, B. Samanta, E. da S. Barboza, C. Sevik, M. Milosevic, D. Cakir, *Phys. Rev. Mater.* **8**, 055002 (2024).

[41] X.-H. Li, H.-L. Cui, R.-Z. Zhang, *Vacuum* **145**, 234 (2017).

[42] H. Zhang, F. Dai, H. Xiang, Z. Zhang, Y. Zhou, *J. Mater. Sci. Technol.* **35**, 530 (2019).

[43] D. Roy, S. Kanojia, K. Mukhopadhyay, N.E. Prasad, *Bull. Mater. Sci.* **44**, (2021).

[44] U.P. Agarwal, *Molecules* **24**, 1659 (2019).

[45] M. Bagheri H.-P. Komsa, *Sci. Data* **10**, (2023).

[46] X. Zhang, Y. Tsujikawa, M. Miyamoto et al., *Phys. Rev. Mater.* **9**, 095001 (2025).

[47] Q. Fan, Y. Li, R. Yang, X. Yu, S. Yun, *Acta Phys. Pol. A* **145**, 273 (2024).

[48] J.-S. Yun, S. Choi, S.H. Im, *Carbon Energy* **3**, 667 (2021).

[49] Y. Sun, A. Yang, Y. Duan, L. Shen, M. Peng, H. Qi, *Int. J. Refract. Met. Hard Mater.* **103**, 105781 (2022).

[50] M.A.S. Sujon, T. Andriollo, A. Islam, *J. Polym. Res.* **30**, 440 (2023).

[51] B. Li, Y. Duan, L. Shen, M. Peng, H. Qi, *Philos. Mag.* **102**, 1628 (2022).

[52] S. Sett, V.K. Aggarwal, A. Singha, A.K. Raychaudhuri, *Phys. Rev. Appl.* **13**, 054008 (2020).

[53] J.P. Perdew, K. Burke, M. Ernzerhof, *Phys. Rev. Lett.* **77**, 3865 (1998).

[54] G. Kresse, J. Furthmüller, *Phys. Rev. B* **54**, 11169 (1996).

[55] G. Kresse, D. Joubert, *Phys. Rev. B* **59**, 1758 (1999).

[56] F. Shimojo, K. Hoshino, Y. Zempo, *Comput. Phys. Commun.* **142**, 364 (2001).

[57] J.M. Skelton, L.A. Burton, A.J. Jackson, F. Oba, S.C. Parker, A. Walsh, *Phys. Chem. Chem. Phys.* **19**, 12452 (2017).

[58] W. Li, J. Carrete, N.A. Katcho, N. Mingo, *Comput. Phys. Commun.* **185**, 1747 (2014).

[59] S.P. Keshri, S.K. Pati, *ACS Appl. Energy Mater.* **5**, 13590 (2022).

[60] L. Lindsay, D.A. Broido, *J. Phys. Condens. Matter* **20**, 165209 (2008).

[61] T. Ouyang, M. Hu, *J. Appl. Phys.* **117**, 245101 (2015).